PHYSICAL REVIEW A **91**, 042509 (2015)

Attosecond-magnetic-field-pulse generation by coherent circular molecular electron wave packets

Kai-Jun Yuan[*] and André D. Bandrauk[†]
Laboratoire de Chimie Théorique, Faculté des Sciences, Université de Sherbrooke, Sherbrooke, Québec, Canada J1K 2R1

(Received 29 October 2014; published 27 April 2015)

Attosecond-magnetic-field-pulse generation is investigated using numerical solutions of the time-dependent Schrödinger equation for oriented $H_2{}^+$ excited and ionized by intense 2×10^{16} W/cm^2 circularly polarized attosecond UV pulses. The results show that localized attosecond-magnetic-field pulses B at the molecular center ($\mathbf{r} = \mathbf{0}$) decrease in intensity with increasing attosecond-pulse wavelength, following a classical model. Magnetic-field minima are obtained at a specific laser-pulse wavelength $\lambda = 55$ nm, which is attributed to ionization suppression. It is found that spatially localized coherent circular electron currents and wave packets are created and induce magnetic-field minima. At $\lambda = 55$ nm, coherent excitation between the ground state and Rydberg states is created, giving rise to partial Rabi oscillations in population and doublets in molecular above-threshold-ionization photoelectron energy spectra. Pulse intensities are shown to influence these effects on the attosecond time scale through population variations.

DOI: 10.1103/PhysRevA.91.042509 PACS number(s): 33.20.Lg, 33.80.Rv, 42.50.Hz

I. INTRODUCTION

Attosecond (1 as $= 10^{-18}$ s) pulses generated from high-order-harmonic generation (HHG) or free-electron lasers offer the possibility of investigating electron dynamics on its natural time scale [1,2]. To date the shortest *linearly* polarized single pulse has been obtained with a duration of 67 as [3]. With intense mid-infrared laser HHG, the generation of even shorter attosecond pulses has been proposed [4]. With such attosecond pulses, electrons in matter can be visualized and controlled on the attosecond time scale and with subnanometer dimension [5–7]. However, the development of attosecond-pulse technology has been limited to linear polarization due to an essential limiting physical principle, electron-ion recollision induced by intense linearly polarized laser pulses, which is generally absent for circular polarization [8,9].We have recently proposed methods of generating *circularly* polarized molecular HHG due to the nonsymmetry of molecular Coulomb potentials [10]. Circularly polarized laser pulses have been used to study total angular momentum conservation in laser-induced femtosecond magnetism [11], emphasizing the role of rotational symmetry breaking in solids. Atomic Coulomb potentials generally prohibit circularly polarized HHG due to their spherical symmetry and strict selection rules, except for specific atomic potentials such as low ionization potentials I_p [12]. Ionization of atoms by intense ultrafast circularly polarized laser pulses has recently been studied theoretically at 800 nm [13–15], showing the importance of excited states.

Femtosecond magnetization phenomena are currently studied with femtosecond circular-polarization x-ray sources due to their nanometer resolution and ultrarapid response shorter than physical relaxation times [16–18]. Recently experiments have shown reversal of magnetism with 40 fs circularly polarized laser pulses [19]. Circularly polarized attosecond pulses should therefore allow the study of the control of magnetic light-matter interactions through laser-induced electron currents on the electron's time scale. We have shown that circularly polarized attosecond pulses allow for the generation of circular attosecond electron currents in matter, resulting in the production of intense attosecond magnetic-field pulses [20]. In the present work, we study the creation of circular molecular coherent electron wave packets (CEWPs) by circularly polarized attosecond laser pulses, thus generating attosecond magnetic-field pulses. Such ultrashort pulses produce different dynamics based on properties of the pulse shape. In the *long-wavelength* intense-field limit, the energy distribution of photoelectrons for linearly polarized light is determined by the phase angle or carrier-envelope phase at which the electron is ionized. The distribution in circularly polarized light, on the other hand, is characteristic of the pulse envelope [21]. By transforming the corresponding Hamiltonian to a circular rotating frame, one obtains an atomic [22,23] or molecular [24] electronic system in the presence of a rotating static field corresponding to the envelope. In the intense-laser *high-frequency* regime, it has been found that pulse ramp (turn on and off) can lead to ionization suppression [25] and/or dynamic interference [26] for intense *linear* polarization. In the present work we report from three-dimensional (3D) time-dependent Schrödinger equation (TDSE) simulations a similar strong dependence of *circular* electron currents and attosecond-magnetic-field-pulse generation on the pulse envelope. Furthermore, we report molecular above-threshold-ionization (MATI) spectra which illustrate splitting of these spectra at particular laser wavelengths. These splittings are shown to be responsible for minima in the intensities of the generated attosecond-magnetic-field pulses, which we attribute to the generation of circular CEWPs.

The paper is arranged as follows: We briefly describe computational methods for numerically solving 3D TDSEs of an aligned molecular ion $H_2{}^+$ by intense circularly polarized attosecond UV laser pulses in Sec. II. The dependence of induced magnetic fields on the pulse wavelengths is numerically simulated in Sec. III. The Rydeberg circular CEWPs lead to splitting in the MATI spectra. In Sec. IV we finally summarize our findings. Throughout this paper, atomic units (a.u.) $e = \hbar = m_e = 1$ are used unless otherwise stated.

---

[*] kaijun.yuan@usherbrooke.ca
[†] andre.bandrauk@usherbrooke.ca

II. NUMERICAL METHODS

We numerically solve the 3D TDSE within a static nuclear (Born-Oppenheimer) frame,

$$i\frac{\partial}{\partial t}\psi(\mathbf{r},t) = H\psi(\mathbf{r},t) \tag{1}$$

in cylindrical coordinates $\mathbf{r} = (\rho,\theta,z)$ with the molecular $\mathbf{R}$ axis and the laser polarization as the (xOy) plane, where $x = \rho\cos\theta$ and $y = \rho\sin\theta$, and O is the origin of the electron coordinates ($\mathbf{r} = \mathbf{0}$) and the molecular center. The 3D TDSE in Eq. (1) is propagated by a high-order split-operator method [27] in the time step δt combined with a fifth-order finite-difference method and Fourier-transform technique in the spatial steps $\delta\rho$, δz, and $\delta\theta$. The time step is taken to be $\delta t =$ 0.01 a.u. = 0.24 as. The spatial discretization is $\delta\rho = \delta z =$ 0.25 a.u. for a radial grid range $0 \leqslant \rho \leqslant 128$ a.u. (6.77 nm) and $|z| \leqslant 32$ a.u. (1.69 nm), and the angle grid size $\delta\theta = 0.025$ rad. The maximum single-cycle classical radius of an ionized electron for $E_0 = 1$ a.u. ($I_0 = 3.5 \times 10^{16}$ W/cm^2) and $\omega =$ 1 a.u. ($\lambda = 45$ nm) is $\alpha_d = E_0/\omega^2 = 1$ a.u. (0.053 nm). This radius increases with increasing number of laser cycles [9]. Thus to prevent unphysical effects due to the reflection of the ionized wave packet from the grid boundary, we multiply $\psi(\rho,\theta,z,t)$ by a "mask function" or absorber in the radial coordinates ρ with the form $\cos^{1/8}[\pi(\rho - \rho_a)/2\rho_{abs}]$. For all results reported here we set the absorber domain $\rho_a =$ $\rho_{max} - \rho_{abs} = 104$ a.u. with $\rho_{abs} = 24$ a.u., greatly exceeding the field-induced oscillation $\alpha_d = E/\omega^2$ of the electron. The exact initial ground electronic orbital for the $X\,^2\Sigma_g^+$ state wave function is obtained by propagating the TDSE without electric fields for an arbitrary initial wave function by "imaginary" time integration [27].

The radiative interaction between the laser field and the electron is described in the length gauge by

$$V_L(\mathbf{r}) = \mathbf{r}\cdot\mathbf{E}(t) = \rho\cos\theta E_x(t) + \rho\sin\theta E_y(t) \tag{2}$$

for circularly polarized pulses, where $\mathbf{E}(t) = Ef(t)[\hat{e}_x\cos(\omega t) + \hat{e}_y\sin(\omega t)]$, propagating in the z direction perpendicular to the molecular (x,y) plane and $\hat{e}_{x/y}$ is the polarization direction. A smooth $\sin^2(\pi t/n\tau)$ pulse envelope $f(t)$ for maximum amplitude E and intensity $I = I_x + I_y = c\varepsilon_0 E^2$ is adopted, where one optical cycle period $\tau = 2\pi/\omega$. This pulse satisfies the total zero area $\int E(t)dt = 0$ in order to exclude static field effects [2]. The time-dependent electron current density is defined by the quantum expression, also in the length gauge,

$$\mathbf{j}(\mathbf{r},t) = \frac{i}{2}[\psi(\mathbf{r},t)\nabla_{\mathbf{r}}\psi^*(\mathbf{r},t) - \psi^*(\mathbf{r},t)\nabla_{\mathbf{r}}\psi(\mathbf{r},t)]. \tag{3}$$

$\psi(\mathbf{r},t)$ is the exact Born-Oppenheimer (static nuclei) electron wave function obtained from the TDSE and $\nabla_{\mathbf{r}} = \mathbf{e}_\rho\nabla_\rho + \mathbf{e}_\theta\frac{1}{\rho}\nabla_\theta + \mathbf{e}_z\nabla_z$ in cylindrical coordinates. Then the corresponding *time-dependent* magnetic field is calculated using the following classical Jefimenko equation [28], taking into account time-dependent currents:

$$\mathbf{B}(\mathbf{r},t) = \frac{\mu_0}{4\pi}\int\left[\frac{\mathbf{j}(\mathbf{r}',t_r)}{|\mathbf{r}-\mathbf{r}'|^3} + \frac{1}{|\mathbf{r}-\mathbf{r}'|^2 c}\frac{\partial\mathbf{j}(\mathbf{r}',t_r)}{\partial t}\right] \times (\mathbf{r}-\mathbf{r}')d^3\mathbf{r}', \tag{4}$$

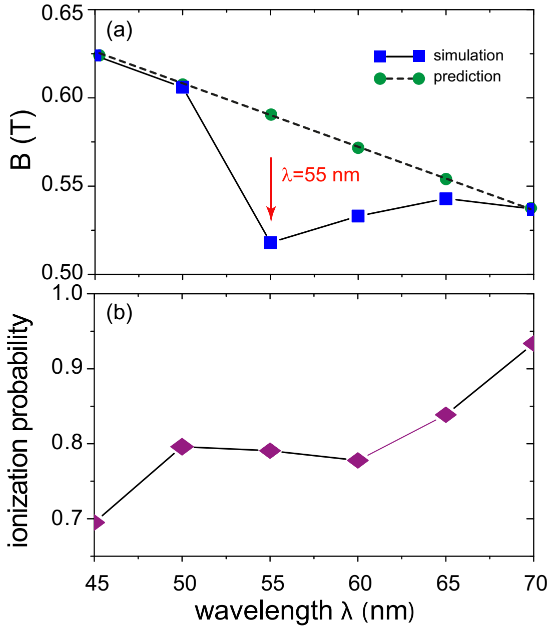

FIG. 1. (Color online) (a) Induced maximum magnetic fields B at the molecular central point O (blue squares) as a function of wavelengths λ of circularly polarized attosecond UV laser pulses. The pulse intensity is fixed at $I = 2 \times 10^{16}$ W/cm^2. The laser parameters and the corresponding values of the induced magnetic fields B are listed in Table I. Green dots are predictions from a classic model, Eqs. (5)–(7). (b) The corresponding ionization probabilities at different pulse wavelengths λ.

where $t_r = t - r/c$ is the retarded time and $\mu_0 = 4\pi \times 10^{-7}$ N A^{-2} (6.692×10^{-4} a.u.). Units of $B(\mathbf{r},t)$ are teslas (1 T = 10^4 G). For the static zero-field time-independent conditions occurring after the pulse, then Eq. (4) reduces to the classical Biot-Savart law [Eq. (4)] [28].

III. RESULTS AND DISCUSSION

Figure 1(a) displays the maximum values of the local magnetic field B (squares) at the molecular central point O generated by five-cycle circularly polarized attosecond UV pulses. We fix the pulse intensity at $I = 2 \times 10^{16}$ W/cm^2, corresponding to 1×10^{16} W/cm^2 in each of the x and y polarization directions. Such high intensity is required for high frequencies. The full width at half maximum (FWHM) of each pulse and the corresponding induced magnetic-field strength are listed in Table I. From Fig. 1(a) one sees that

TABLE I. Maximum values of the induced magnetic fields B (T) at the central point O of the x-oriented molecular ion H_2^+ by circularly polarized UV laser pulses with different intensities I (units of I_0), wavelengths λ (nm), and FWHM (as). ($I_0 = 2 \times 10^{16}$ W/cm^2.)

λ (nm)		45	50	55	60	65	70
FWHM (as)		372	418	460	492	540	576
B (T)	I_0	0.624	0.606	0.518	0.533	0.543	0.537
	$0.5I_0$	0.442	0.482	0.459	0.398	0.419	0.369
	$0.1I_0$	0.152	0.186	0.217	0.228	0.209	0.186

the attosecond-magnetic-field pulse is critically sensitive to the pulse wavelength. At $\lambda = 45$ nm ($\omega = 1$ a.u.) below the $H_2{}^+$ ionization $I_p = 1.1$ a.u. at $R_e = 2$ a.u., the strongest magnetic field is produced with $B = 0.624$ T. As the pulse wavelength λ increases and the photon energy ω decreases further, the induced magnetic field B decreases. At $\lambda = 55$ nm ($\omega = 0.82$ a.u.), a minimum is obtained for $B = 0.518$ T. On increasing the pulse wavelength λ further, B increases as well. At $\lambda = 65$ nm ($\omega = 0.69$ a.u.), $B = 0.543$ T. However, we note that at $\lambda = 70$ nm ($\omega = 0.64$ a.u.), the magnetic field decreases again to $B = 0.537$ T.

Using a classical model for a moving point charge [9], the corresponding classical magnetic field

$$\mathbf{B} = \frac{\mu_0}{4\pi}\frac{\mathbf{v}\times\mathbf{r}_0}{|\mathbf{r}|^2}, \tag{5}$$

where $\mathbf{r}_0$ is the unit vector pointing along $\mathbf{r}$, depends on the velocities $\mathbf{v}$ and displacements $\mathbf{r}$ of charges with respect to the molecular center O. With ultrashort pulses at wavelengths and photon energies $\omega \lesssim I_p$, where $I_p = 1.1$ a.u. is the molecular ionization potential, the electron is released from the molecule with low initial velocities by absorbing one photon due to the broad spectral width of the attosecond pulses. Assuming zero initial electron velocities $\dot{x}(t_0) = \dot{y}(t_0) = 0$, where t_0 is the ionization time, the laser-induced time-dependent velocities are [9,21]

$$\begin{aligned}\dot{x}(t) &= -\frac{E}{\omega}(\sin\omega t - \sin\omega t_0),\\ \dot{y}(t) &= -\frac{E}{\omega}(\cos\omega t_0 - \cos\omega t)\end{aligned} \tag{6}$$

We note that, with $t_0 = 0$, the average velocity $\langle\dot{x}(t)\rangle = 0$, whereas $\langle\dot{y}(t)\rangle = -E/\omega$ is nonzero and is called the drift velocity perpendicular to the ionization [21]. The corresponding displacements are

$$\begin{aligned}x(t) &= -\frac{E}{\omega^2}[\cos\omega t_0 - \cos\omega t - (\omega t - \omega t_0)\sin\omega t_0],\\ y(t) &= -\frac{E}{\omega^2}[\sin\omega t_0 - \sin\omega t + (\omega t - \omega t_0)\cos\omega t_0].\end{aligned} \tag{7}$$

From Eqs. (6) and (7) it is found that decreasing the pulse frequency ω or increasing the wavelength λ leads to increase of the maximum induced electron velocity $v = 2E/\omega$, and the corresponding radii

$$r_{n'} = \frac{2E}{\omega^2}[1 + (n' + 1/2)^2\pi^2]^{1/2}, \quad n' = 0,1,2,\ldots \tag{8}$$

at $\omega t - \omega t_0 = (2n' + 1)\pi$ [9]. From Eqs. (5)–(7) one then gets the localized maximum field

$$B \sim \frac{v}{r_{n'}} \sim \omega f(\omega t_0,\omega t), \tag{9}$$

where the factor $f(\omega t_0,\omega t)$ is given by

$$f(\omega t_0,\omega t) = \sqrt{\frac{2 - 2\cos\phi}{2 - 2\cos\phi - 2\phi\sin\phi + \phi^2}}, \tag{10}$$

with phase $\phi = \omega t - \omega t_0$. In Eq. (10) one sees that the factor $f(\omega t_0,\omega t)$ is independent of the pulse frequency ω for maximum fields, i.e., the phase ϕ is a constant. Therefore, an increase of wavelength λ or lower ω results in a monotonic decrease of the magnetic field due mainly to the larger radii $r_{n'}$ of the electron, as illustrated in Fig. 1(a) (green dots). However the numerical results in Fig. 1 show a minimum in the magnetic-field intensity at $\lambda = 55$ nm, which is not consistent with the model predictions $\sim\omega$ in Eqs. (5)–(7). The dip mainly results from ionization suppression. As shown in Eqs. (3) and (4) the magnetic field depends on the electron current $\mathbf{j}(\mathbf{r},t)$, which decreases with decreasing ionization probability. In Fig. 1(b) we present the ionization probabilities as a function of the pulse wavelength λ. Increasing λ leads to an increase of the ionization probability which then decreases at $\lambda = 55$ and 60 nm. As λ is further raised, the ionization probability increases rapidly thereafter.

For the attosecond laser pulse of FWHM 460 as at $\lambda = 55$ nm, the corresponding spectral width at half maximum is about $\Delta\omega = 0.3$ a.u. Assuming that the excited states are dense with energy spacing much less than 0.3 a.u., a well-localized circularly polarized electronic wave packet can be expected to be created from the excitation of the multiple Rydberg states during the excitation and ionization processes [22]. In Fig. 2 we plot the density of the electron wave packet around the pulse peak time, $\mathcal{P}(x,y) = |\psi(x,y,t)|^2$, and its corresponding momentum distribution after a Fourier transform, $\mathcal{P}(p_x,p_y) = |\psi(p_x,p_y,t)|^2$. One sees that the excited wave packets are mainly localized around the molecular center O, i.e., $x = y = 0$, Fig. 2(a), and double humps appear in the momentum distribution, Fig. 2(b). The distributions of the excited electron wave packets rotate counterclockwise, following the polarization of the ionizing circularly polarized UV pulses. This indicates that the electron motions obey the classical models in Eqs. (6) and (7). At the beginning of the pulse, the doublets are strongly asymmetric. With increase of excitation, the splitting enhances gradually. At $t = 3\tau = 552$ as one sees that a symmetric doublet is obtained. The evolution of doublets reflects the localization of CEWPs, which is the essence of the ionization suppression. The trapping effects by creation of resonant Rydberg states lead to Rabi oscillations in population, thus giving rise to the minimum of the magnetic field B at the molecular center O.

To examine the localization of the CEWPs in Rydberg states, we analyze the energy of the induced electron currents at different wavelengths λ. Figure 3 displays the corresponding photoelectron energy spectral $\mathcal{J}(E_e)$, obtained from Eq. (3) at an asymptotic point $\rho_0 = 100$ a.u. before the absorption domain. After a Fourier transform one then gets the resolved energy of the currents $\mathcal{J}(E_e)$ [29]. From Fig. 3 one sees that double peaks are produced in the photoelectron energy spectra around energies $E_{en} = (n+1)\omega - I_p$, corresponding to MATI. At the specific wavelength $\lambda = 55$ nm pronounced symmetric doublets are obtained with energy interval $\Delta E \simeq 0.3$ a.u., as illustrated in Fig. 3(c). The splitting in electron current energy spectra agrees well with the distribution $\mathcal{P}(p_x,p_y)$ of excited electron wave packets in Fig. 2(b). However, on increasing or decreasing λ, the doublets become asymmetric. At the shortest $\lambda = 45$ nm and the longest $\lambda = 70$ nm the asymmetric doublets nearly disappear.

In Fig. 4 we show the evolutions of population in the ground $X^2\Sigma_g^+$ state of $H_2{}^+$ at the different wavelengths used in Figs. 1–3. At the shorter wavelengths $\lambda = 45$ nm and 50 nm, there is partial population transfer out of the ground state

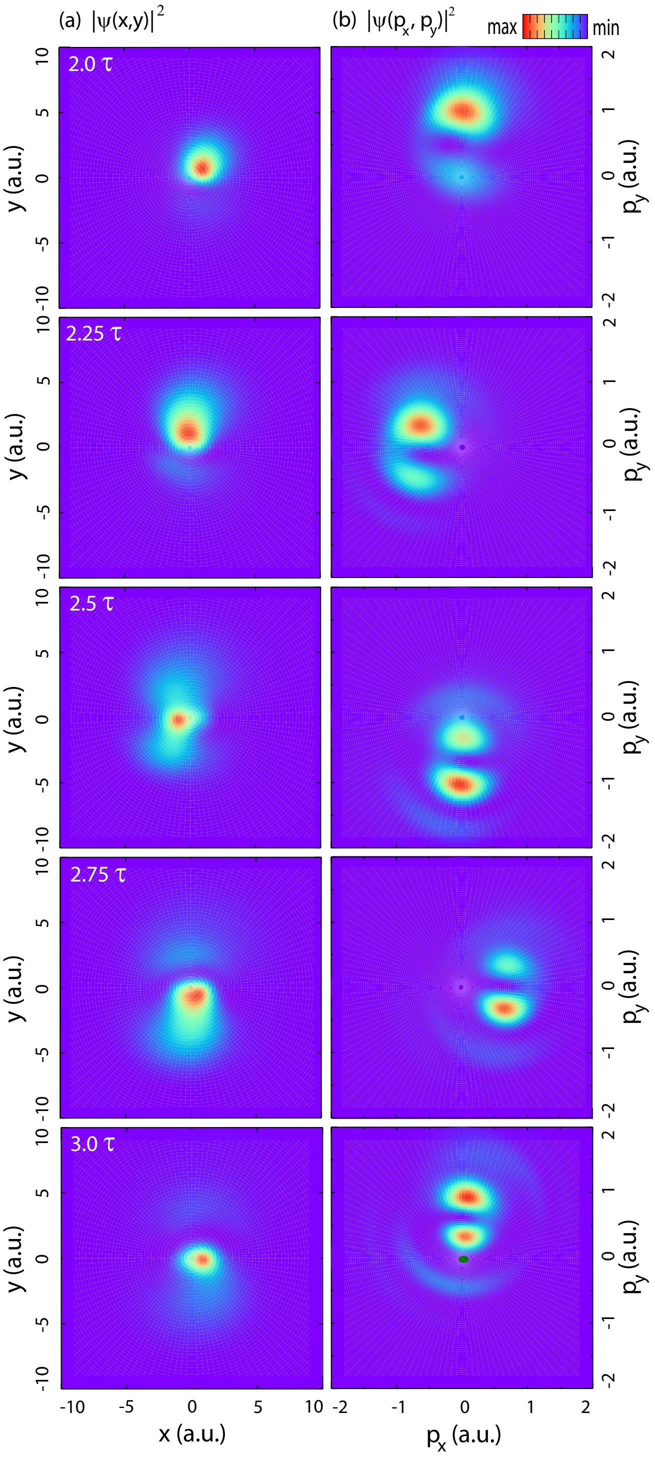

FIG. 2. (Color online) Density distributions of circular CEWPs in (a) coordinate $|\psi(x,y)|^2$ and (b) momentum $|\psi(p_x,p_y)|^2$ space at different times ranging from $t = 2\tau = 368$ as to $3\tau = 552$ as for $I = 2\times10^{16}$ W/cm^2, $\lambda = 55$ nm, and FWHM of 460 as circularly polarized UV laser pulses.

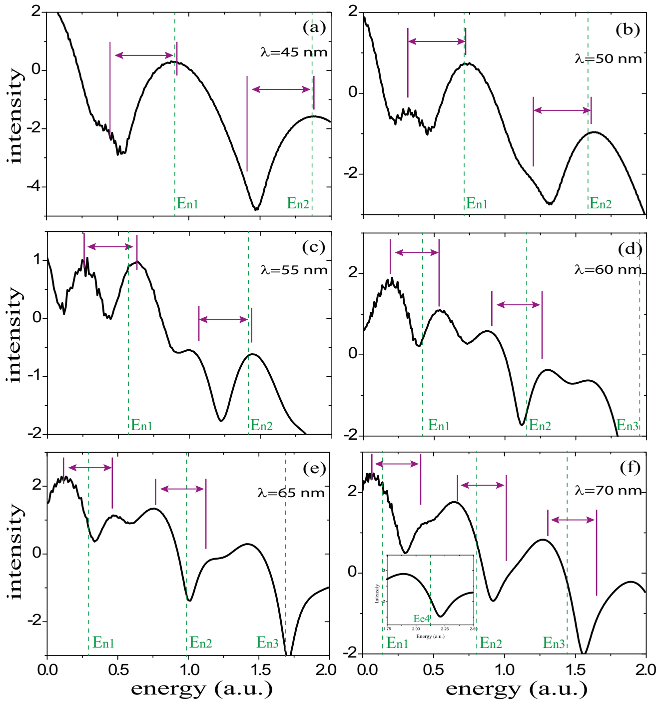

FIG. 3. (Color online) Photoelectron energy spectra $\mathcal{J}(E_e)$ of x-oriented $H_2{}^+$ at an asymptotic point $\rho_0 = 100$ a.u. for intense $I = 2\times10^{16}$ W/cm^2 circularly polarized attosecond UV pulses at different wavelengths and durations, corresponding to Fig. 1 and Table I. Dotted lines present classical photoelectron kinetic energies $E_{en} = (n+1)\omega - I_p$. Inset in panel (f) shows the MATI spectra around the photoelectron energy $E_{e4} = 5\omega - I_p$.

up to 30% at 45nm. On increasing the pulse wavelength, complete population transfer occurs. The population first decreases completely to zero and then recovers to a fixed value 0.2 with the circularly polarized attosecond laser pulse at wavelength $\lambda = 55$ nm. We have chosen short wavelengths $\lambda \sim 45$ nm or corresponding high frequencies $\omega \sim 1$ a.u. ($\tau = 152$ as) in order to restrict the induced electron currents to $r_n = 1$ a.u. (0.053 nm), i.e., atomic-molecular subnanometer dimensions, thus generating strong magnetic fields $B \sim \omega$ as discussed above. High-frequency strong-field electron dynamics differs from low-frequency dynamics and is more simply treated in a space translation or acceleration representation of laser-matter interaction, in which Kramers-Henneberger (KH) time-averaged potentials lead to strong deformations of atomic [25,30] or molecular [31] Coulomb potentials.

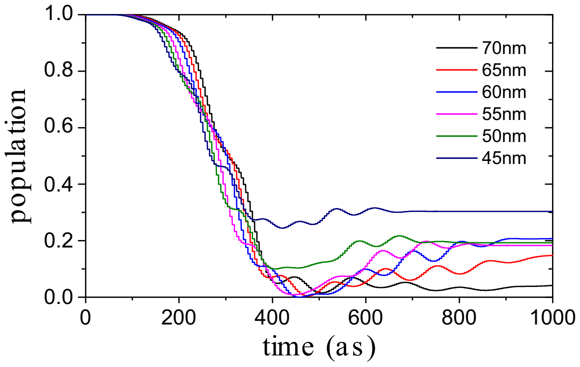

FIG. 4. (Color online) Evolutions of population with time of the $H_2{}^+$ ground $X\,{}^2\Sigma_g^+$ electronic state with circularly polarized attosecond UV laser pulses of intensity $I = 2\times10^{16}$ W/cm^2 at different wavelengths λ (cf. Figs. 1 and 3).

Electrons at such high frequencies become localized at their maximum excursions $\alpha_d = E/\omega^2$, resulting in positive shifts of their bound-state energies [25,30,31]. Thus one expects high-frequency MATI peaks to move to high energies, in contrast to the high-intensity low-frequency case where ac-Stark shifts are negative [30,32,33]. The MATI spectra illustrated in Fig. 3 show that each MATI peak is a doublet, with one peak lower and the other higher in energy around the central energies $E_{en} = n\omega - I_p$. Furthermore, Fig. 4 demonstrates complete depletion of the ground state at $\lambda < 60$ nm ($\omega > 0.75$ a.u.), well below the ionization potential $I_p = 1.1$ a.u. ($\lambda = 40$ nm). The partial recovery of the ground-state population before the end of the pulse we ascribe to incomplete single-cycle Rabi oscillations which can occur with short intense laser pulses [34,35].

It is of note that the strong ionization limits complete recovery of the ground-state population so that a complete Rabi oscillation cannot occur. As an example, in Fig. 4 at the specific wavelength $\lambda = 55$ nm ($\omega = 0.82$ a.u.), a half-period Rabi oscillation leads to zero ground-state population at $t \approx 460$ as (the peak time of the pulses), corresponding to the MATI splitting $\Delta\omega = 0.3$ a.u., i.e., Rabi frequency $\Delta\tau = 2\pi/\Delta\omega = 500$ as. At 65 and 70 nm, resonance with the $2p\pi_u$ state occurs, thus increasing the ionization during the pulse turn as seen in Fig. 1(b), and hence suppressing Rabi effects. Using rectanglelike pulses allows identification of a much weaker ground-state population maximum. Similarly, with five-cycle pulses, one observes repopulation and localization. The MATI peak doublets reported in Fig. 3 reflect coherence of the attosecond electron wave packets where the Rabi effect is strongest, i.e., for wavelengths $60 > \lambda > 50$ nm, resulting in depletion of the ground state and suppression of ionization but also a minimum in the magnetic field, Fig. 1(a). A Floquet-state analysis of the KH states for an atom has shown that ionization suppression in linear-polarization high-frequency short pulses is caused by the appearance of laser-induced resonance states [25]. Figures 2–4 suggest the creation of such states with intense circularly polarized attosecond pulses as coherent electron currents which control the intensity of the generated attosecond-magnetic-field pulses (Fig. 1).

Finally we show the effects of the pulse intensity on the induced magnetic field B and photoelectron energy spectra. Figure 5 illustrates the pulse-wavelength- (λ-) dependent magnetic field B at the molecular center O at two weaker intensities $I = 1 \times 10^{16}$ W/cm^2 and 2×10^{15} W/cm^2. The other pulse parameters are the same as those used in Fig. 1. The values of the induced magnetic field B at O are listed in Table I. It is found that on decreasing the pulse intensity to $I = 1 \times 10^{16}$ W/cm^2 a minimum occurs at $\lambda = 60$ nm due to the coherent CEWPs in Rydberg states. However, as the pulse intensity decreases further Rabi oscillation cannot be triggered between the ground and Rydberg states. As a result the minimum vanishes at the lower intensity $I = 2 \times 10^{15}$ W/cm^2. In Fig. 6 we also illustrate the corresponding photoelectron energy spectra at $\lambda = 55$ nm and 60 nm. The splitting doublets in Fig. 3 become more strongly asymmetric at $I = 1 \times 10^{16}$ W/cm^2 and then disappear at 2×10^{15} W/cm^2. The pulse intensity dependence confirms the importance of the coherent excited CEWPs in the generation of induced magnetic fields B and the photoelectron energy spectra.

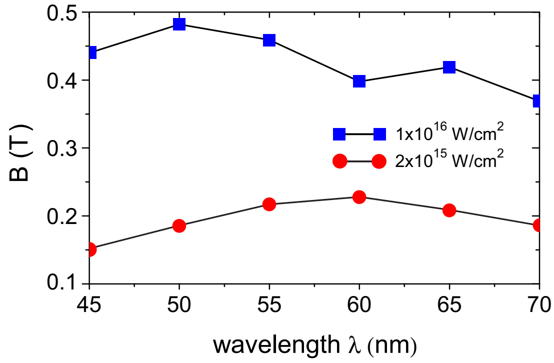

FIG. 5. (Color online) Dependence of induced maximum magnetic fields B at the molecular central point O at wavelengths λ for circularly polarized UV laser pulses with intensities (blue squares) $I = 1 \times 10^{16}$ W/cm^2 and (red circles) 2×10^{15} W/cm^2. The laser parameters and the corresponding values of the induced magnetic fields B are listed in Table I.

IV. CONCLUSIONS

In summary, attosecond-magnetic field-pulses can be generated in oriented H_2^+ by intense 2×10^{16} W/cm^2 circularly polarized few-cycle UV laser pulses, which produce circular electron currents with radii of atomic dimensions as predicted by Eqs. (8) and (9). Numerical results from nonperturbative solutions to 3D TDSEs show that the induced ultrashort magnetic field is critically sensitive to the pulse wavelength λ. At $\lambda = 55$ nm, field minima occur, which are attributed to ionization suppression effects caused by localized circular CEWPs. We find that with few-cycle pulses at $\lambda = 55$ nm circularly polarized CEWPs of Rydberg states can be created, leading to partial Rabi oscillations and MATI doublets in

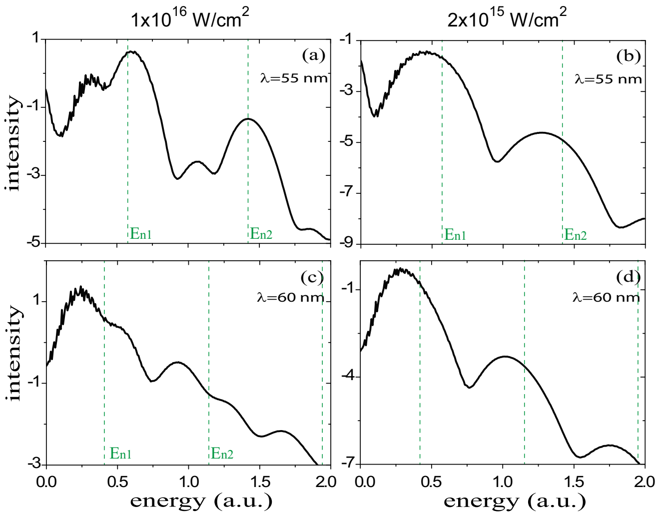

FIG. 6. (Color online) Photoelectron energy spectra $\mathcal{J}(E_e)$ of x-oriented H_2^+ at an asymptotic point $\rho_0 = 100$ a.u. for circularly polarized attosecond UV pulses of intensity [left column (a),(c)] $I = 1 \times 10^{16}$ W/cm^2 and [right column (b),(d)] 2×10^{15} W/cm^2 at two different wavelengths [top row (a),(b)] $\lambda = 55$ nm and [bottom row (c),(d)] 60 nm. The dotted lines present classical photoelectron kinetic energies $E_{en} = (n + 1)\omega - I_p$.

energy spectra. Suppression of partial ionization reduces attosecond-magnetic-field generation. The effects of pulse intensities are also presented. At weak intensity, no magnetic-field minimum occurs. Therefore the minimum of the magnetic field B and the doublets of the photoelectron energy spectra arising from coherent CEWPs appear only with proper laser-pulse parameters.

ACKNOWLEDGMENTS

K.J.Y. is grateful for helpful discussions with Zhigang Sun (DICP, China). The authors also thank RQCHP and Compute Canada for access to massively parallel computer clusters and NSERC and FQRNT for financial support in their ultrafast science programs.

[1] P. B. Corkum and F. Krausz, Nat. Phys. **3**, 381 (2007).
[2] F. Krausz and M. Ivanov, Rev. Mod. Phys. **81**, 163 (2009).
[3] K. Zhao, Q. Zhang, M. Chini, Y. Wu, X. Wang, and Z. Chang, Opt. Lett. **37**, 3891 (2012).
[4] T. Popmintchev *et al.*, Science **336**, 1287 (2012).
[5] S. Chelkowski, G. L. Yudin, and A. D. Bandrauk, J. Phys. B **39**, S409 (2006).
[6] H. Niikura, D. M. Villeneuve, and P. B. Corkum, Phys. Rev. Lett. **94**, 083003 (2005).
[7] H. C. Shao and A. F. Starace, Phys. Rev. Lett. **105**, 263201 (2010).
[8] P. B. Corkum, Phys. Rev. Lett. **71**, 1994 (1993).
[9] K. J. Yuan and A. D. Bandrauk, J. Phys. B **45**, 074001 (2012).
[10] K. J. Yuan and A. D. Bandrauk, Phys. Rev. Lett. **110**, 023003 (2013).
[11] G. P. Zhang and T. F. George, Phys. Rev. B **78**, 052407 (2008).
[12] F. Mauger, C. Chandre, and T. Uzer, Phys. Rev. Lett. **104**, 043005 (2010); **105**, 083002 (2010).
[13] I. Barth and O. Smirnova, Phys. Rev. A **84**, 063415 (2011).
[14] C. H. Raymond Ooi, W. L. Ho, and A. D. Bandrauk, Phys. Rev. A **86**, 023410 (2012).
[15] J. H. Bauer, F. Mota-Furtado, P. F. O'Mahony, B. Piraux, and K. Warda, Phys. Rev. A **90**, 063402 (2014).
[16] C. H. Lambert *et al.*, Science **345**, 1337 (2014).
[17] B. Vodungbo *et al.*, Nat. Commun. **3**, 999 (2007).
[18] G. P. Zhang, W. Hübner, G. Lefkidis, Y. Bai, and T. F. George, Nat. Phys. **5**, 499 (2009); G. P. Zhang, Y. Bai, W. Hübner, G. Lefkidis, and T. F. George, J. Appl. Phys. **103**, 07B113 (2008).
[19] C. D. Stanciu, F. Hansteen, A. V. Kimel, A. Kirilyuk, A. Tsukamoto, A. Itoh, and Th. Rasing, Phys. Rev. Lett. **99**, 047601 (2007).
[20] K. J. Yuan and A. D. Bandrauk, Phys. Rev. A **88**, 013417 (2013).
[21] P. B. Corkum, N. H. Burnett, and F. Brunel, Phys. Rev. Lett. **62**, 1259 (1989).
[22] M. Kalinski and J. H. Eberly, Phys. Rev. Lett. **77**, 2420 (1996).
[23] A. F. Brunello, T. Uzer, and D. Farrelly, Phys. Rev. Lett. **76**, 2874 (1996).
[24] T. Zuo and A. D. Bandrauk, J. Nonlin. Opt. Phys. Mater. **04**, 533 (1995); A. D. Bandrauk and H. Z. Lu, Phys. Rev. A **68**, 043408 (2003).
[25] D. Barash, A. E. Orel, and R. Baer, Phys. Rev. A **61**, 013402 (1999); T. Sako, J. Adachi, A. Yagishita, M. Yabashi, T. Tanaka, M. Nagasono, and T. Ishikawa, *ibid.* **84**, 053419 (2011).
[26] P. V. Demekhin and L. S. Cederbaum, Phys. Rev. Lett. **108**, 253001 (2012).
[27] A. D. Bandrauk and H. Shen, J. Chem. Phys. **99**, 1185 (1993); A. D. Bandrauk and H. Z. Lu, J. Theor. Comput. Chem. **12**, 1340001 (2013).
[28] O. D. Jefimenko, *Electricity and Magnetism: An Introduction to the Theory of Electric and Magnetic Fields*, 2nd ed. (Electret Scientific Co., Star City, WV, 1989); Am. J. Phys. **58**, 505 (1990).
[29] K. J. Yuan, H. Lu, and A. D. Bandrauk, Phys. Rev. A **83**, 043418 (2011); K. J. Yuan and A. D. Bandrauk, *ibid.* **85**, 053419 (2012).
[30] D. Bauer and F. Ceccherini, Phys. Rev. A **66**, 053411 (2002).
[31] T. Zuo and A. D. Bandrauk, Phys. Rev. A **51**, R26(R) (1994).
[32] L. Y. Peng and A. F. Starace, Phys. Rev. A **76**, 043401 (2007).
[33] L. Y. Peng, E. A. Pronin, and A. F. Starace, New J. Phys. **10**, 025030 (2008).
[34] Z. Sun and N. Lou, Phys. Rev. Lett. **91**, 023002 (2003).
[35] A. Palacios, H. Bachau, and F. Martín, Phys. Rev. A **74**, 031402(R) (2006).